Mon. Not. R. Astron. Soc. **000**, 000–000 (0000) Printed 7 March 2024 (MN LATEX style file v2.2)

A Gemini Snapshot Survey for Double Degenerates⋆

Mukremin Kilic[1], Warren R. Brown[2], A. Gianninas[1]†, Brandon Curd[1,3], Keaton J. Bell[4], and Carlos Allende Prieto[5,6]
[1]*Department of Physics and Astronomy, University of Oklahoma, 440 W. Brooks St., Norman, OK, 73019, USA*
[2]*Smithsonian Astrophysical Observatory, 60 Garden St, Cambridge, MA 02138, USA*
[3]*Department of Astronomy, Harvard University, 60 Garden St, Cambridge, MA 02138, USA*
[4]*Department of Astronomy, University of Texas at Austin, Austin, TX 78712, USA*
[5]*Instituto de Astrofísica de Canarias, E-38205 La Laguna, Tenerife, Spain*
[6]*Departamento de Astrofísica, Universidad de La Laguna, E-38206 La Laguna, Tenerife, Spain*

arXiv:1707.08948v1 [astro-ph.SR] 27 Jul 2017

7 March 2024

ABSTRACT

We present the results from a Gemini snapshot radial-velocity survey of 44 low-mass white dwarf candidates selected from the Sloan Digital Sky Survey spectroscopy. To find sub-hour orbital period binary systems, our time-series spectroscopy had cadences of 2 to 8 min over a period of 20-30 min. Through follow-up observations at Gemini and the MMT, we identify four double degenerate binary systems with periods ranging from 53 min to 7 h. The shortest period system, SDSS J123549.88+154319.3, was recently identified as a subhour period detached binary by Breedt and collaborators. Here we refine the orbital and physical parameters of this system. High-speed and time domain survey photometry observations do not reveal eclipses or other photometric effects in any of our targets. We compare the period distribution of these four systems with the orbital period distribution of known double white dwarfs; the median period decreases from 0.64 to 0.24 d for $M = 0.3 - 0.5 M_{\odot}$ to $M < 0.3 M_{\odot}$ white dwarfs. However, we do not find a statistically significant correlation between the orbital period and white dwarf mass.

Key words: binaries: close — white dwarfs — stars: individual (SDSS J083446.91+304959.2, J123549.88+154319.3, J123728.64+491302.6, J234248.86+081137.2) — supernovae: general — gravitational waves

1 INTRODUCTION

There are now more than 90 short period binary white dwarfs known (e.g., Saffer et al. 1988; Bragaglia et al. 1990; Marsh et al. 1995; Moran et al. 1997; Maxted et al. 2000; Morales-Rueda et al. 2005; Nelemans et al. 2005; Vennes et al. 2011; Rebassa-Mansergas et al. 2017; Breedt et al. 2017), including more than three dozen systems that will merge within a Hubble time. The majority of the merger systems were found in the last 7 years, thanks to the Extremely Low Mass Survey (the ELM Survey, Brown et al. 2016a, and references therein), which targets white dwarfs with $\log g < 7$ and $M < 0.3 M_{\odot}$. Given the finite age of the universe, the only way to form ELM white dwarfs is through binary evolution, and we do in fact find almost 100% of ELM white dwarfs in short period systems. This is significantly higher than the binary fraction of 10% for the overall population of white dwarfs that were observed as part of the Supernova-Ia Progenitor

⋆ Based on observations obtained at the Gemini, MMT, and the Apache Point observatories. Gemini is operated by the Association of Universities for Research in Astronomy, Inc., under a cooperative agreement with the NSF on behalf of the Gemini partnership: the National Science Foundation (United States), the National Research Council (Canada), CONICYT (Chile), the Australian Research Council (Australia), Ministério da Ciência, Tecnologia e Inovação (Brazil) and Ministerio de Ciencia, Tecnología e Innovación Productiva (Argentina). The MMT is a joint facility of the Smithsonian Institution and the University of Arizona. The Apache Point Observatory 3.5-meter telescope is owned and operated by the Astrophysical Research Consortium. This paper includes data taken at The McDonald Observatory of The University of Texas at Austin.
† Visiting astronomer, Kitt Peak National Observatory, National Optical Astronomy Observatory, which is operated by the Association of Universities for Research in Astronomy (AURA) under a cooperative agreement with the National Science Foundation.

© 0000 RAS

surveY (SPY, Napiwotzki et al. 2004; Maoz & Hallakoun 2017).

Brown et al. (2016b) estimate an ELM white dwarf merger rate of 3×10^{-3} yr^{-1} over the entire disk of the Milky Way. This is significantly larger than the AM CVn formation rate, indicating that most ELM white dwarf systems will merge. These merger systems, depending on the total mass of the binary, will likely form single subdwarfs, extreme helium stars, or single massive white dwarfs. The most likely outcome is an R Cor Bor star, since the ELM white dwarf merger rate is statistically identical to the R Cor Bor formation rate. These merger rates are dominated by the quickest merger systems, the ones with the shortest periods.

There are currently five sub-hour orbital period detached double white dwarfs known; J0106−1000, J0651+2844, J1630+4233, WD 0931+444 (Kilic et al. 2014, and references therein), and J1235+1543 (Breedt et al. 2017). The two shortest period systems with $P < 20$ min, J0651+2844 and WD 0931+444, are verification sources for the *Laser Interferometer Space Antenna* (*LISA*, Kilic et al. 2015; Korol et al. 2017). The discovery of additional sub-hour orbital period systems is important for both precise white dwarf merger rate estimates and future space-based gravitational wave missions (Amaro-Seoane et al. 2012).

Here we present the results from a targeted search for sub-hour period binary white dwarfs from Gemini Observatory, with additional follow-up observations from the MMT. We discuss our target selection in Section 2, describe our follow-up spectroscopy and photometry in Section 3, and present the orbital solutions for four binaries in Section 4, including J1235+1543. Breedt et al. (2017) independently identified the latter as a sub-hour orbital period system based on the SDSS subspectra. Here we refine the orbital parameters of this system based on extended follow-up observations. We discuss the parameters of the four confirmed binary systems in our sample, as well as the implications of the results from this search in Section 5.

2 TARGET SELECTION

Figure 1 shows the temperature versus period distribution of the binary white dwarfs in the ELM Survey (Brown et al. 2016a). This figure demonstrates that the shortest period systems also happen to be the hotter white dwarfs with $T_{\rm eff} > 12{,}000$ K. This is a direct consequence of gravitational wave emission: white dwarfs in the shortest period systems merge before they have a chance to cool down. Hence, we only see them when they are relatively young and hot. This provides an excellent, but currently under-utilized, selection mechanism for the shortest period binary systems. For example, 39% of the previously observed ELM white dwarfs hotter than 12,000 K are in binaries with $P < 0.1$ d, with a median period of 65 min.

We take advantage of this selection mechanism to search for short period binary white dwarfs in the SDSS Data Release 10 spectroscopy sample. One of the authors (CAP) fitted all of the DR10 optical spectra with stellar templates for main-sequence stars (Castelli & Kurucz 2004) and white dwarfs using the `FERRE` code (Allende-Prieto & Apogee Team 2015). Among these objects, we identify 49 relatively hot low-mass white dwarfs with $T_{\rm eff} > 12{,}000$ K, $M < 0.4 M_{\odot}$, S/N>10 SDSS spectroscopy, and with no previous radial velocity observations. Note that our target selection would have included the eclipsing double white dwarf systems J0651 (Brown et al. 2011) and CSS 41177 (Parsons et al. 2011).

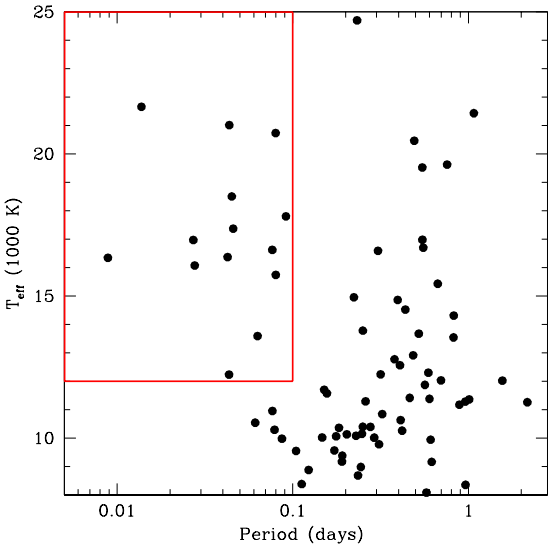


Figure 1. Temperature versus orbital period distribution for the binary white dwarfs in the ELM Survey. Roughly 39% of the previously known ELM white dwarfs with $T_{\rm eff} > 12{,}000$ K are in binaries with $P < 0.1$ d (red box).

3 OBSERVATIONS

We obtained follow-up optical spectroscopy of 34(10) targets using the 8m Gemini North (South) telescope equipped with the Gemini Multi-Object Spectrograph (GMOS) as part of the programs GN-2016A-Q-54, GN-2016B-Q-45, GS-2015A-Q-10, GS-2016A-Q-58, and GS-2016B-Q-48. Since we are only interested in finding sub-hour orbital period systems, and not constraining the binary periods for all targets, we limited our observations to ≈30 min per target. Depending on the target brightness, we obtained a sequence of 4-11 × 2-8 min long exposures with the B600 grating and a 0.5″ slit, providing wavelength coverage from 3570 Å to 6430 Å and a resolving power of 1850 for GMOS-North, and coverage from 3620 Å to 6780 Å and a resolving power of 1940 for GMOS-South. Each spectrum has a comparison lamp exposure taken within 10 min of the observation time.

Based on the initial velocity measurements from GMOS, we obtained additional follow-up data for six targets (J1113+2712, J1237+4913, J1323+3254, J1407+1241, J1633+3030, and J1716+2838) using the same setup on Gemini North as part of the Fast Turnaround program GN-2016A-FT-34. Most of these targets were observed with back-to-back exposures over ≈1.8 h, but some of the observations were split into multiple nights due to weather conditions and the constraints imposed by queue scheduling.

We used the 6.5m MMT with the Blue Channel spectrograph to obtain follow-up data on five targets (J0834+3049,

J1032+2147, J1235+1543, J1237+4913, and J2342+0811) between 2016 Jan and 2017 Mar. We operated the spectrograph with the 832 line mm^{-1} grating in second order, providing wavelength coverage from 3600 Å to 4500 Å and a spectral resolution of 1.0 Å. We obtained all observations at the parallactic angle, with a comparison lamp exposure paired with every observation. We flux-calibrated using blue spectrophotometric standards (Massey et al. 1988).

We also used the Kitt Peak National Observatory 4m telescope + KOSMOS (Martini et al. 2014) in 2016 Dec and the Apache Point Observatory 3.5m telescope with the Dual Imaging Spectrograph (DIS) in 2017 Mar to obtain additional follow-up spectroscopy of J1237+4913. We operated the KOSMOS (as part of the program 2016B-0160) and DIS spectrographs with the b2k and B1200 gratings, providing wavelength coverages of 3500-6200 Å and 3750-5000 Å, and spectral resolutions of 2.0 Å and 1.8 Å, respectively.

We obtained follow-up time-series photometry of one of our targets, J1235+1543, using the McDonald Observatory 2.1m Otto Struve telescope with the ProEM camera and the BG40 filter. We used an exposure time of 10 s with a total integration time of 3230 s, which covers the entire orbital period for this short period system. We binned the CCD by 4 × 4, which resulted in a plate scale of 0.38″ pixel^{-1}. We adopted the external IRAF package *ccd_hsp* (Kanaan et al. 2002) for aperture photometry. There was only one bright comparison star available in the field of view, and we corrected for transparency variations by dividing the sky-subtracted light curve by the light curve of this comparison star.

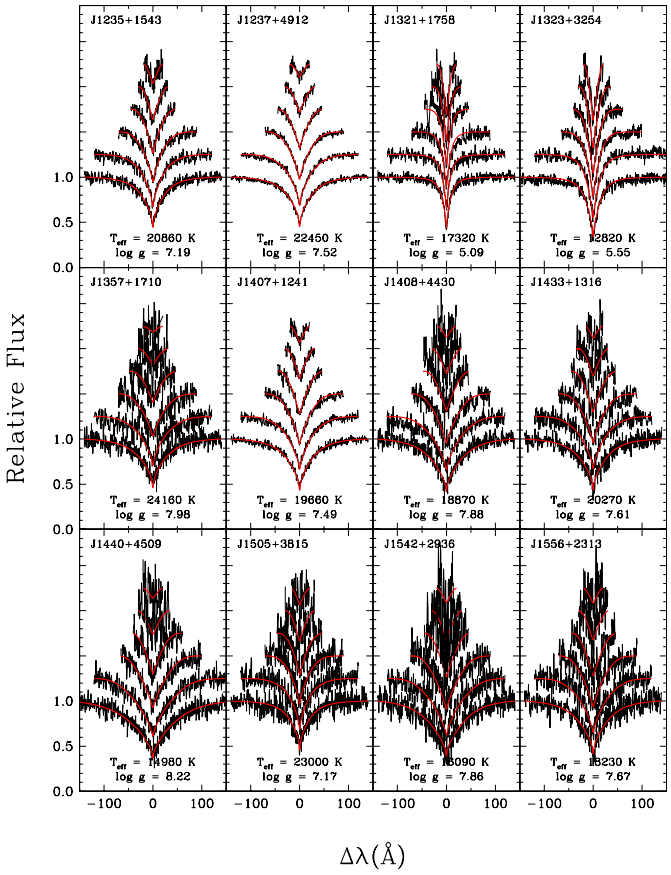


Figure 2. 1D model fits (red) to the observed Balmer line profiles (black) from Gemini spectra for 12 of the targets in our sample. We fit the lines from Hβ (bottom) to H9 (top) using pure hydrogen model atmospheres.

4 RESULTS

4.1 Stellar Atmosphere Fits

We employed a pure-hydrogen model atmosphere grid covering 4000-35,000 K and $\log g = 4.5$-9.5 to fit the normalized Balmer line profiles of our targets in the summed, rest-frame Gemini spectra. The models and our fitting procedures are described in Gianninas et al. (2015). We used the evoluationary sequences from Althaus et al. (2013) for low-mass He-core white dwarfs and Fontaine et al. (2001) for C/O core white dwarfs to estimate masses and absolute magnitudes for each object.

Figure 2 shows our model fits to a dozen targets in our sample. Given our initial target selection ($T_{\rm eff} \geqslant 12{,}000$ K) based on the SDSS data, this figure uses the hot solution in the model fits. Balmer lines are strongest at $T_{\rm eff} \sim 14{,}000$ K for average mass C/O white dwarfs. This usually leads to a degeneracy in the best-fit solution for model atmosphere analysis where a hot and a cool solution can both fit the normalized Balmer line profiles reasonably well, but optical photometry can help identify the correct solution in the majority of the cases. Five of our targets have *ugriz* photometry that implies an effective temperature below 10,000 K. Using the cool solutions in our spectroscopic model fits, these five objects (J1113+2712, J1321+1758, J1323+3254, J1011+0242, and J1132+0751) are best-fit with $T_{\rm eff} \leqslant 9{,}000$K and $\log g < 7$ models, i.e. sdA stars (Kepler et al. 2016). Brown et al. (2017) demonstrate that ∼99% of the sdA stars are metal-poor main-sequence stars in the halo. Hence, we do not consider these five stars as white dwarfs.

Table 1 presents the physical parameters for all 44 stars in our sample. Our model atmosphere analysis shows that nine of these stars have masses above $0.5 M_{\odot}$. Excluding these nine stars and the sdAs, there are 30 low-mass white dwarfs in our sample.

4.2 Radial Velocities and Errors

We measure radial velocities by cross-correlating the spectra against high signal-to-noise templates of known velocity. We use the RVSAO package documented in Kurtz & Mink (1998) and based on the Tonry & Davis (1979) algorithm. The cross-correlation is the normal product of the Fourier transform of an object spectrum with the conjugate of the Fourier transform of a template spectrum. The software package includes extra steps such as Fourier bandpass filtering, to dampen the high frequency (pixel-to-pixel) and low frequency (slow continuum roll) noise in spectra.

Velocity errors are measured from the full-width-at-half-maximum of the cross-correlation peak using the *r*-statistic (Tonry & Davis 1979). Empirical validation us-

Table 1. Physical parameters and the summary of radial velocity measurements for our targets. The top 34 and the bottom 10 objects were observed at Gemini North and South, respectively.

Object SDSS	g_0 (mag)	$T_{\rm eff}$ (K)	$\log g$ (cm s^{-2})	M ($M_\odot$)	N	Mean (km s^{-1})	χ^2	$\log_{10}(p)$
J073708.56+360215.0	19.08	23840 ± 630	7.50 ± 0.08	0.43 ± 0.03	6	−76.6 ± 28.3	18.93	−2.70
J073835.56+324121.6	19.55	23080 ± 730	7.69 ± 0.10	0.48 ± 0.05	6	10.4 ± 30.7	32.81	−5.39
J074928.74+364451.6	19.06	24630 ± 710	7.89 ± 0.11	0.58 ± 0.06	6	67.5 ± 37.2	7.93	−0.80
J080024.85+393757.6	19.08	25580 ± 480	7.84 ± 0.07	0.55 ± 0.04	6	25.9 ± 27.7	14.86	−1.96
J082239.40+114142.7	18.75	25580 ± 460	7.45 ± 0.07	0.43 ± 0.03	5	−30.9 ± 21.1	5.98	−0.70
J083446.91+304959.2	18.78	17680 ± 380	7.06 ± 0.07	0.29 ± 0.01	18	210.4 ± 7.5	228.98	−38.4
J090730.65+381754.0	17.83	22260 ± 280	7.25 ± 0.04	0.38 ± 0.01	8	−69.3 ± 15.0	26.10	−3.32
J091844.51+120948.1	17.92	18090 ± 190	7.39 ± 0.03	0.39 ± 0.02	7	83.9 ± 13.9	3.18	−0.10
J103232.94+214712.3	18.21	15760 ± 260	7.47 ± 0.05	0.40 ± 0.02	29	24.6 ± 5.0	58.06	−3.14
J111303.59+271259.0	18.53	8890 ± 290	5.56 ± 0.16	...	12	54.8 ± 10.6	24.43	−1.96
J113117.50+374740.1	18.55	22600 ± 370	7.37 ± 0.05	0.40 ± 0.02	6	−22.8 ± 19.0	7.11	−0.67
J120020.71+682019.8	18.36	15360 ± 460	7.62 ± 0.07	0.44 ± 0.03	6	80.8 ± 30.4	7.32	−0.70
J123549.88+154319.3	17.19	20860 ± 230	7.19 ± 0.03	0.35 ± 0.01	39	−8.0 ± 4.1	774.3	−137
J123728.64+491302.6	18.50	22450 ± 130	7.52 ± 0.02	0.43 ± 0.02	41	−56.6 ± 6.1	283.2	−37.6
J132153.51+175806.1	17.26	8070 ± 50	5.95 ± 0.17	...	11	190.2 ± 12.4	9.31	−0.30
J132350.96+325444.5	19.43	9100 ± 30	5.17 ± 0.16	...	18	−150.9 ± 7.9	27.71	−1.31
J135715.36+171032.1	19.00	24160 ± 460	7.98 ± 0.06	0.62 ± 0.04	6	47.7 ± 23.9	7.03	−0.66
J140714.50+124153.8	19.19	19660 ± 150	7.49 ± 0.02	0.42 ± 0.02	18	−12.8 ± 8.7	48.21	−4.10
J140821.99+443008.0	18.97	18870 ± 350	7.88 ± 0.06	0.56 ± 0.04	6	−12.3 ± 22.9	5.00	−0.38
J143315.47+131654.0	19.17	20270 ± 370	7.61 ± 0.05	0.45 ± 0.03	4	−48.3 ± 21.0	3.22	−0.44
J144023.92+450938.2	19.16	14980 ± 380	8.22 ± 0.05	0.75 ± 0.04	4	31.7 ± 27.4	14.00	−2.54
J150546.21+381554.2	18.84	23000 ± 520	7.17 ± 0.07	0.36 ± 0.02	5	−110.6 ± 24.0	2.47	−0.19
J154230.67+293606.3	18.60	16090 ± 450	7.86 ± 0.08	0.54 ± 0.05	5	15.6 ± 29.2	1.97	−0.13
J155657.69+231358.5	18.68	18230 ± 380	7.67 ± 0.06	0.46 ± 0.03	4	25.4 ± 19.1	8.41	−1.42
J163338.88+303041.7	18.16	18740 ± 110	7.30 ± 0.02	0.37 ± 0.01	24	−120.7 ± 6.9	35.26	−1.31
J170816.36+222551.0	19.07	22900 ± 770	7.14 ± 0.10	0.34 ± 0.03	4	−52.6 ± 26.6	10.20	−1.77
J171602.17+283852.3	18.94	17700 ± 120	7.69 ± 0.02	0.46 ± 0.02	18	−7.2 ± 9.3	37.84	−2.59
J172850.05+581316.3	18.52	23790 ± 610	7.51 ± 0.08	0.43 ± 0.03	5	−61.9 ± 22.9	1.93	−0.13
J201154.21−104124.1	18.90	22530 ± 770	7.95 ± 0.10	0.60 ± 0.06	5	73.1 ± 31.3	10.99	−1.57
J210252.10+010108.6	18.20	22980 ± 270	7.59 ± 0.04	0.45 ± 0.02	5	105.1 ± 16.3	3.85	−0.37
J221426.78+055025.8	18.66	22090 ± 450	7.22 ± 0.06	0.37 ± 0.02	5	−46.2 ± 19.0	24.76	−4.25
J224750.14+295145.1	19.25	22150 ± 480	8.05 ± 0.06	0.66 ± 0.04	5	−39.2 ± 28.2	29.20	−5.15
J234212.47+005121.0	19.30	17230 ± 340	7.53 ± 0.06	0.42 ± 0.03	5	−5.3 ± 19.8	6.87	−0.84
J234248.86+081137.2	18.32	22030 ± 230	7.45 ± 0.03	0.42 ± 0.02	25	12.5 ± 5.7	239.3	−36.7
J000437.66−055731.4	19.03	14220 ± 210	7.76 ± 0.03	0.48 ± 0.03	5	−30.8 ± 14.8	8.53	−1.13
J011258.36−005952.4	18.57	18720 ± 120	7.55 ± 0.02	0.43 ± 0.02	5	53.3 ± 12.1	1.98	−0.13
J031504.58−065727.2	17.45	19120 ± 120	7.48 ± 0.02	0.41 ± 0.02	9	61.0 ± 11.3	5.75	−0.17
J091911.72+082004.4	19.26	25040 ± 360	7.29 ± 0.05	0.39 ± 0.02	6	27.2 ± 16.3	8.27	−0.85
J101132.73+024216.4	18.81	8900 ± 70	6.50 ± 0.16	...	4	325.1 ± 29.9	0.26	−0.01
J103702.02+032648.0	18.29	23400 ± 400	7.25 ± 0.05	0.38 ± 0.02	8	109.3 ± 19.2	14.67	−1.39
J113218.41+075103.0	16.94	7010 ± 30	6.78 ± 0.07	...	9	37.9 ± 14.0	4.60	−0.10
J123717.06−003900.1	19.46	16020 ± 350	8.02 ± 0.06	0.63 ± 0.04	6	71.0 ± 29.0	1.54	−0.04
J154647.28−005003.5	17.68	21410 ± 430	7.46 ± 0.06	0.42 ± 0.02	8	51.7 ± 18.3	16.19	−1.63
J162024.40−000545.9	17.03	21160 ± 260	7.43 ± 0.04	0.41 ± 0.02	13	30.7 ± 14.2	23.68	−1.65

ing repeat low- and high-spectral resolution observations of galaxies and stars confirm the precision of the cross-correlation errors (Kurtz & Mink 1998). However, systematic errors can arise from poorly-matched templates, which skew the shape of the cross-correlation peak.

We address this systematic issue by shifting-to-rest-frame and summing together all observations of a given target, and then cross-correlating the individual spectra against the summed spectrum of itself. This approach minimizes systematic error, but hides statistical error. The location of a star on the spectrograph slit changes how it illuminates the spectrograph and disperses its light onto the detector. We use our higher resolution and higher signal-to-noise ratio MMT data to investigate this issue. Back-to-back exposures of constant velocity targets at the MMT demonstrate a 10 to 15 km s^{-1} dispersion slit illumination effect, most apparent in targets observed in sub-arcsec seeing with short exposure times (like J1235+1543). Wavelength calibration errors also contribute. The MMT arc line fits have 3 km s^{-1} residuals, however the blue end <3900 Å is anchored by weak lines that have larger 5 to 10 km s^{-1} residuals. The cross-correlation does not discriminate between slit illumination and wavelength calibration errors and real velocity change. The upshot is that we must add statistical error in quadrature to the cross-correlation error.

Our approach is to add 20 km s^{-1} in quadrature to the velocity errors of objects observed at Gemini and MMT and 30 km s^{-1} in quadrature to the velocity errors of objects observed at KPNO and APO. When fitting orbital parameters to the confirmed binaries, this choice of errors yields reduced χ^2 values of 1 (see the discussion in Section 4.4). We also test for zero point offsets between telescopes when fitting binary orbital parameters. We see no evidence for zero point offsets greater than the 1-σ error in γ, the systemic velocity.

4.3 Constraints on Radial Velocity Variability

Maxted et al. (2000) presented a robust method for identifying radial velocity variable objects. They used the weighted mean radial velocity for each star in their sample to calculate the χ^2 statistic for a constant-velocity model. They then calculated the probability, p, of obtaining the observed value of χ^2 or higher from random fluctuations of a constant

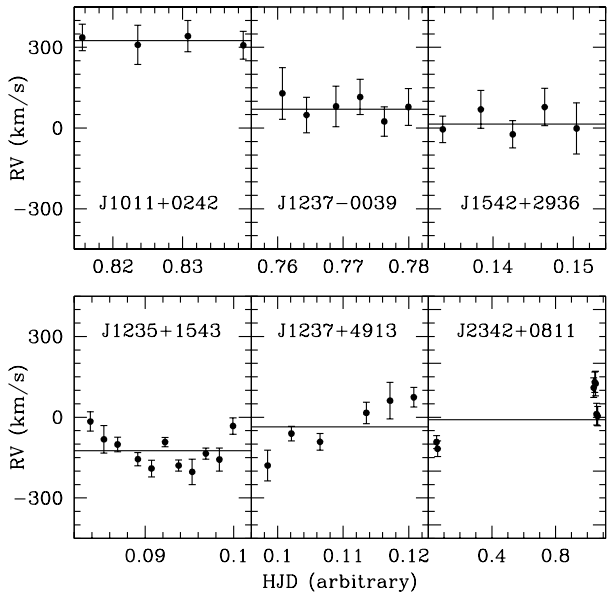


Figure 3. Radial velocity measurements for 3 non-variable (top panels) and 3 variable (bottom panels) objects observed at Gemini North and South. The solid line shows the average velocity for each star.

velocity, taking into account the appropriate number of degrees of freedom. They identify objects with $\log(p) < -4$ as binary systems. This selection leads to a false detection rate of $< 0.5\%$ in a sample of 44 objects.

We adopt the same method to identify radial velocity variable objects in our sample. Table 1 lists the number of spectra (N), weighted mean radial velocity, χ^2 for a constant-velocity fit, and the probability of obtaining this χ^2 value given the number of degrees of freedom ($N-1$) for each star. The majority of the stars in our sample do not show significant velocity variations. Given the brevity of our Gemini observations (except for the stars with extensive follow-up observations), this is not surprising.

Figure 3 shows our initial set of Gemini observations for six stars, three of which are excellent examples of non-velocity-variable objects. Our Gemini data for J1011+0242, J1237−0039, and J1542+2936 (top panels) are consistent with a constant velocity fit with $\log(p) = -0.01$ to -0.13. On the other hand, there are several targets with $\log(p) < -4$, indicating that they are likely in short period binary systems (bottom panels). For example, our 2 min cadence data on J1235+1543 sample a significant portion of the binary orbit, and our 8 min cadence data on J1237+4913 reveal a positive velocity trend in that system. Similarly, the initial set of Gemini observations on J2342+0811 reveal a ≈250 km s^{-1} velocity change over two consecutive nights. We discuss these three objects further in the next section.

The five sdA stars in our sample (J1113+2712, J1321+1758, J1323+3254, J1011+0242, and J1132+0751) do not show significant velocity variations in our data. Metal-poor main sequence stars in detached binaries must have orbital periods above about 9 hr (Brown et al. 2017). Hence, the lack of significant velocity variations in these stars, as well as the majority of the stars in our sample of low-mass white dwarfs is consistent with the expectation that they are likely in longer period binary systems.

4.4 Four Binary Systems

There are eight objects in Table 1 with $\log(p) < -4$; a constant velocity model is a poor representation of the data for these stars. These are likely binary systems. We have limited follow-up data on four of them, J0738+3241, J1407+1241, J2214+0550, and J2247+2951, and we are unable to constrain the orbital parameters for these four systems. However, the remaining four stars with $\log(p) < -4$ have extensive follow-up observations, and they do show significant radial velocity variations with periods ranging from 53 min to 7 h.

We determine orbital parameters by minimizing χ^2 for a circular orbit. Figures 4 and 5 show the radial velocity observations, phased velocity curves, and periodograms for these four white dwarfs. Each panel also includes a blow-up of the frequency range where the minimum χ^2 is found. Morales-Rueda et al. (2003) discussed the problems with identifying the correct orbital period from radial velocity data given problems with aliasing. They found that the reduced χ^2 values from circular orbit fits were significantly larger than 1 for some of their targets. They attributed this to an unaccounted source of error in their velocity measurements, perhaps the true variability of the star or slit illumination effects. They estimated the level of this uncertainty in their data such that when systematic and statistical errors are added in quadrature they give reduced χ^2 values of 1. We estimate statistical uncertainties of 20 and 30 km s^{-1} for the Gemini/MMT and KPNO/APO data, respectively (Section 4.2). Adding the cross-correlation errors from RVSAO and the statistical uncertainties in quadrature, we find the best-fit circular orbits with reduced χ^2 ranging from 0.97 to 1.16 for our four binary systems.

Out of these four binaries, three have unique orbital period solutions, while J2342+0811 has a significant period alias (at $P = 0.14369 \pm 0.0029$ d and $K = 126.0 \pm 10.1$ km s^{-1}). Its second period alias at $P = 5$ h differs by 20 in χ^2 and is unlikely to be significant. The χ^2 minima have substructure due to the sampling (see the insets in Figures 4 and 5), however we do not fit the substructure. We measure the orbital period from the envelope of χ^2, which is well-defined and symmetric in all four binaries.

We estimate errors by re-sampling the radial velocities with their errors and re-fitting orbital parameters 10,000 times. This Monte Carlo approach samples χ^2 space in a self-consistent way. We report the median period, semi-amplitude, and systemic velocity along with the average 15.9% and 84.1% percentiles of the distributions in Table 2. The distributions are symmetric, and so we average the percentiles for simplicity. We also fit J2342+0811's second and third minima at $P = 3.5$ and 5 hr; the semi-amplitudes differ by 2 km s^{-1} and are thus statistically identical to the best fit.

Table 2 presents the orbital elements for these four binary systems with well constrained orbits. Note that Breedt et al. (2017) also identified J1235+1543 as a subhour orbital period binary with $P = 49.5$ min and $K = 176 \pm 21$ km s^{-1}. However, they only used 5 radial velocity measurements from 800-1000 s long exposures. Based on 39 expo-

Table 2. Orbital Parameters

SDSS	P (d)	K (km s^{-1})	γ (km s^{-1})	$\chi^2_{\rm red}$	f ($M_\odot$)	M_1 ($M_\odot$)	M_2 ($M_\odot$)	$\tau_{\rm merge}$
J0834+3049	0.30079 ± 0.0011	179.3 ± 13.9	183.3 ± 8.5	1.16	0.1789	0.29	⩾0.47	⩽13 Gyr
J1235+1543	0.03672 ± 0.0014	166.5 ± 6.2	10.5 ± 5.0	1.03	0.0176	0.35	⩾0.17	⩽98 Myr
J1237+4913	0.10763 ± 0.0024	143.6 ± 10.5	−45.1 ± 7.0	0.97	0.0334	0.43	⩾0.25	⩽1.0 Gyr
J2342+0811	0.16788 ± 0.0014	128.3 ± 10.9	9.1 ± 10.4	1.06	0.0367	0.42	⩾0.26	⩽3.3 Gyr

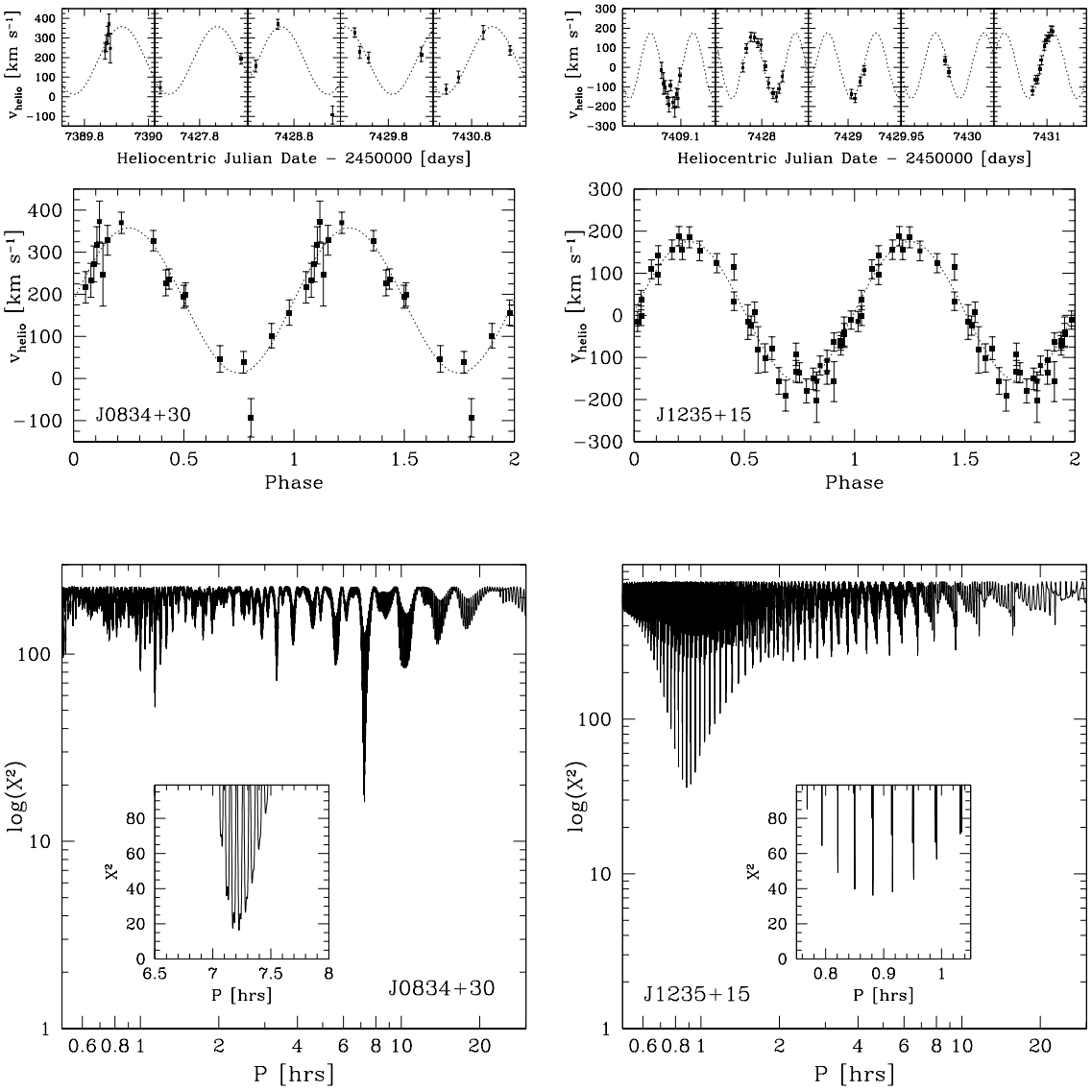


Figure 4. Radial velocity observations, phased velocity curves, and periodograms for J0834+3049 and J1235+1543. Insets show the distribution of χ^2 around the minima on a linear scale.

sures, with exposure times as short as 2 min, we refine the period and velocity semi-amplitude for J1235+1543 to $P = 52.9$ min and $K = 166.5 \pm 6.2$ km s^{-1}.

The observed velocity semi-amplitudes are relatively modest ($K < 200$ km s^{-1}) for these stars, even for the 53 min period system J1235+1543. The median semi-amplitude of the ELM white dwarf binaries is 220 km s^{-1}(Brown et al. 2016b). However, our targets are about twice as massive as the typical ELM white dwarfs, hence the observed smaller velocity amplitudes are not surprising.

Table 2 also presents the mass functions, constraints on the companion masses, and the merger times due to gravitational wave radiation. Note that we define the visible low-mass white dwarf in each system as the primary star. The minimum mass companions to our targets range from 0.17 to 0.47 $M_\odot$, with gravitational wave merger times of roughly

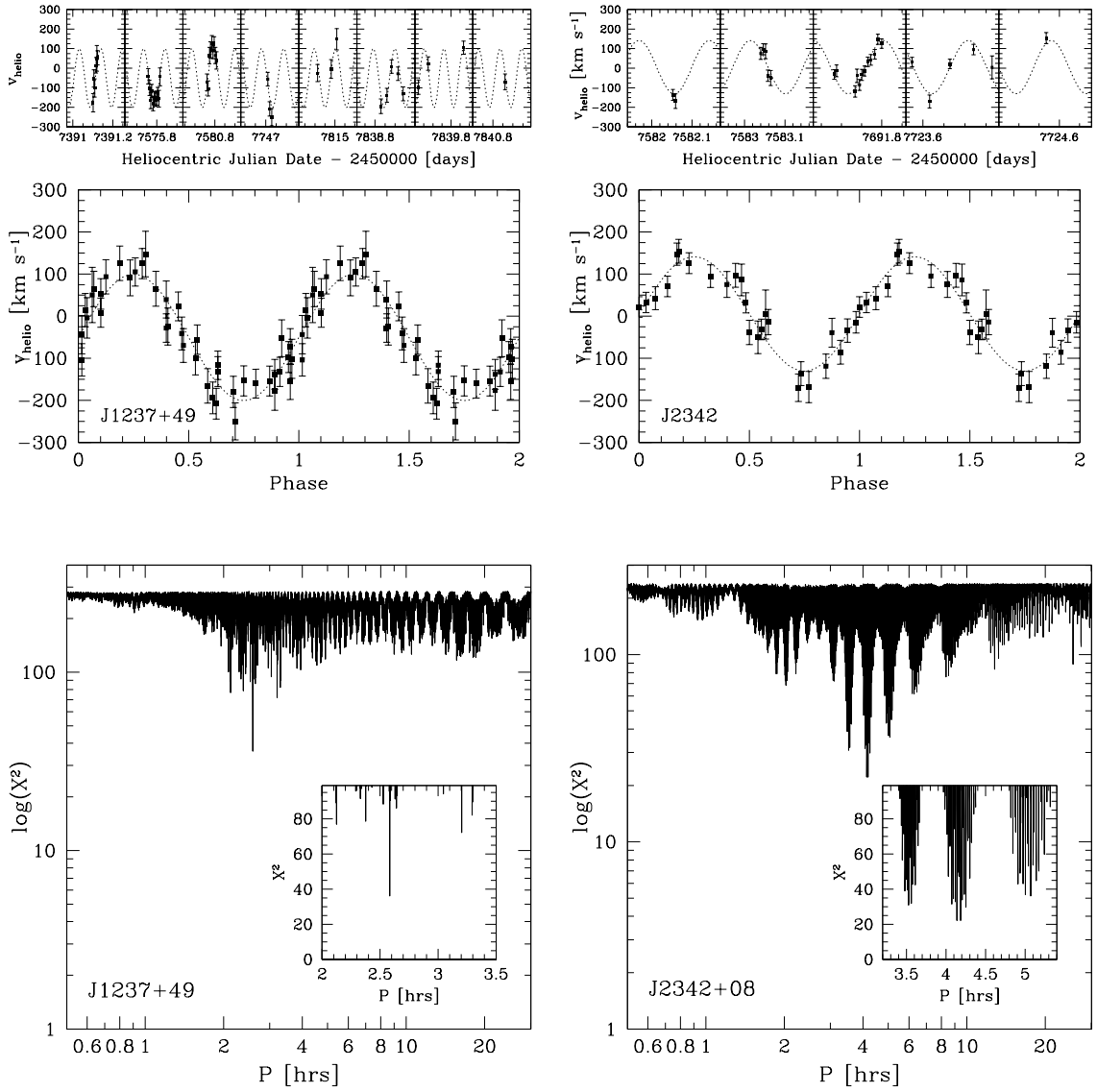


Figure 5. Same as Figure 4, but for J1237+4913 and J2342+0811.

100 Myr for J1235+1543 to ⩽13 Gyr for J0834+3049. All but one of these objects, J0834+3049, have minimum mass companions that are smaller in mass than the visible white dwarfs. Since lower mass white dwarfs should form last, and hence appear brighter, these three single-lined spectroscopic binary systems are likely low inclination systems where the companions are more massive than the visible white dwarfs.

4.5 Photometric Constraints

Spectral types and temperatures of the companions to single-lined spectroscopic binaries can be inferred through photometric effects like Doppler boosting, ellipsoidal variations, and eclipses, or through excess flux in the red or infrared bands. Based on our model atmosphere analysis, the absolute magnitudes of our four binary white dwarfs range from 9.9 to 10.4 in the i-band. If the companions are M dwarfs, the minimum mass companions would be comparable in brightness (within a factor of two, Kroupa & Tout 1997) or even brighter than our white dwarf targets in the i-band. We do not see that. Hence, these four binary systems are double degenerates.

The probability of eclipses increases with decreasing orbital period. To search for eclipses and other photometric effects, we obtained high-speed photometry of the shortest period system in our sample, J1235+1543, with a cadence of 10 s. Figure 6 shows these observations over a binary orbit. There is no significant variability in this system, ruling out eclipses and ellipsoidal variations. The amplitude of the ellipsoidal effect is proportional to $(M_2/M_1)(R_1/a)^3$, where a is the orbital semi-major axis and R_1 is the radius of the primary (Shporer et al. 2010). Compared to the ELM white dwarfs that show ellipsoidal variations (Hermes et al. 2014; Bell et al. 2017), (M_2/M_1) and R_1 are relatively small for J1235+1543. Therefore, the lack of ellipsoidal variations is not surprising.

All four of the binary white dwarfs in our sample were

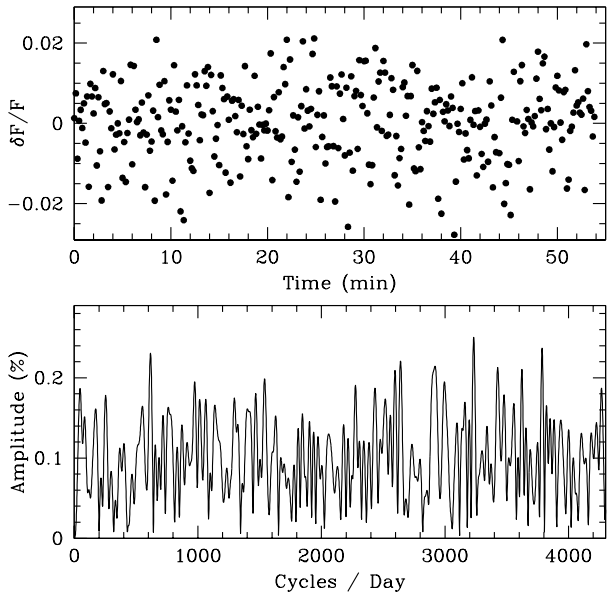


Figure 6. High speed photometry of J1235+1543 over 54 min (top panel) and its Fourier Transform (bottom panel). This short period binary does not show any significant variability.

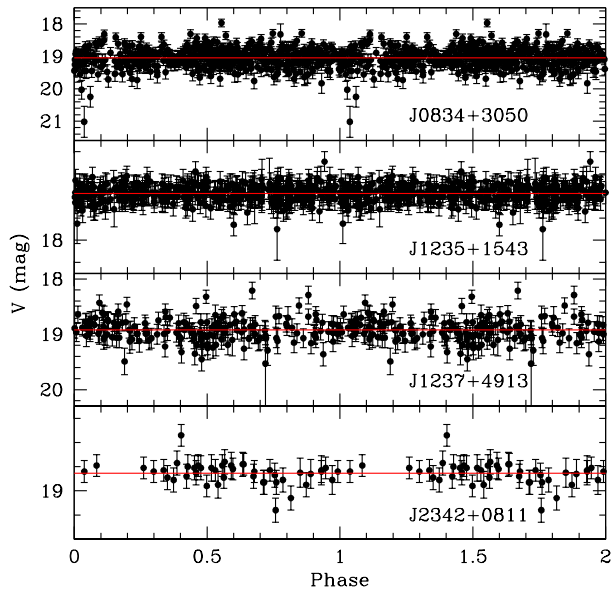


Figure 7. Catalina Sky Survey light curves for the four binary white dwarfs in our sample.

observed by the Catalina Sky Survey (Drake et al. 2009). Figure 7 shows these light curves phased with the best-fit period from the radial velocity data. The Catalina data are sparse for J2342+0811 and part of the orbit is not covered. In addition, the data are noisy for these relatively faint stars. There is a 4σ dip in the J0834+3050 light curve that might be an eclipse, however there are several other $> 4\sigma$ outliers in the same light curve. We suspect that the photometric errors are underestimated. We conclude that there is no significant evidence for eclipses or other photometric effects in any of these systems given the Catalina observations.

5 DISCUSSION

Our snapshot radial velocity survey of relatively hot and young low-mass white dwarfs has revelaed four double degenerates with periods ranging from 53 min to about 7 h. Figure 8 compares the mass and period distribution for these systems against the period distribution of ELM (Brown et al. 2016b) and low-mass white dwarfs (Nelemans et al. 2005; Brown et al. 2011; Debes et al. 2015; Hallakoun et al. 2016; Breedt et al. 2017; Rebassa-Mansergas et al. 2017). The dashed line shows the predicted mass (of the brighter white dwarf) versus period relation from the rapid binary-star evolution (BSE) algorithm of Hurley et al. (2002) for an initial binary of main-sequence stars with masses $2M_{\odot} + 1M_{\odot}$.

The BSE calculations depend on two important parameters, $\alpha_{\rm CE}$ and $\alpha_{\rm int}$ (or $\alpha_{\rm rec}$). The former parameter is the efficiency in converting orbital energy into kinetic energy to eject the envelope, and the latter describes the fraction of the internal energy (thermal, radiation and recombination energy) used to eject the envelope. Note that the latest version of the BSE code treats the binding energy parameter λ as a variable. Zorotovic et al. (2010, 2014), Toonen & Nelemans (2013), and Cojocaru et al. (2017) demonstrate that both of these efficiency parameters are small. We adopt $\alpha_{\rm CE} = \alpha_{\rm rec} = 0.25$ as in Zorotovic et al. (2010, 2014) for the evolutionary sequence shown in Figure 8. The BSE calculations demonstrate that the closest stellar pairs that survive the common-envelope evolution should form lower mass white dwarfs. This is also consistent with the binary population synthesis calculations of Nelemans et al. (2005, see their Figure 8).

Studying the orbital period distribution of post-common-envelope binaries containing C/O and He-core white dwarfs separately, Zorotovic et al. (2011) found median periods of 0.57 d and 0.28 d for the two samples respectively. This difference is consistent with our understanding of the common-envelope evolution. If the mass transfer starts when the primary star is on the red giant branch, this leads to a He-core white dwarf, whereas if the mass transfer starts while the primary is on the asymptotic giant branch, this leads to a C/O core white dwarf. Hence, stellar evolution theory predicts the C/O core white dwarfs in post-common-envelope binaries to be in longer period systems.

The period distribution of the double white dwarfs presented in Figure 8 shows a trend with mass, at least in the observed lower limit in period. The shortest period binaries with $\sim 0.4M_{\odot}$ white dwarfs are in 0.1 d systems, whereas the shortest period 0.2-0.3 $M_{\odot}$ white dwarfs are in 0.01 d systems. The median period decreases from 0.64 d to 0.24 d for $M = 0.3 - 0.5M_{\odot}$ to $M < 0.3M_{\odot}$ white dwarfs in Figure 8. With masses ranging from 0.29 to 0.43 $M_{\odot}$, the period distribution for the four binaries presented in this paper is consistent with the period distribution of the post-common-envelope binaries presented here. The rest of the low-mass white dwarfs in our sample are also likely in binary systems with ∼day long periods. However, our Gemini snapshot survey is not sensitive to such long periods.

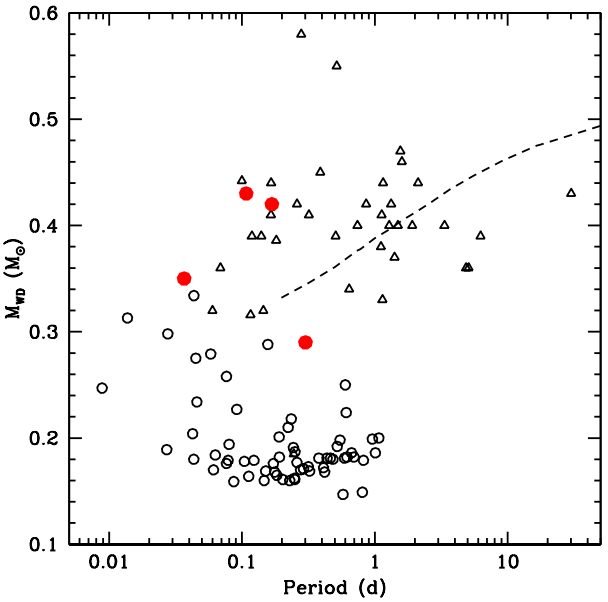


Figure 8. Mass versus period distribution for ELM white dwarfs (open circles), low-mass white dwarfs (open triangles), and the four binary systems presented in this paper (filled circles). The dashed line shows the results from the rapid binary-star evolution (BSE) algorithm of Hurley et al. (2002) for a $2M_\odot + 1M_\odot$ main-sequence binary.

Zorotovic et al. (2011) looked for a significant correlation between the white dwarf mass and orbital period for He-core and C/O-core white dwarfs separately, but they could not reject the null hypothesis based on an F-test. Adding the low-mass white dwarfs from this paper, the ELM Survey, and the literature (the sample shown in Figure 8) does not change the results; we still cannot reject the null hypothesis (no correlation with mass) based on an F-test of the current binary white dwarf sample. This is almost certainly due to the fact that the sample of long period systems with high masses is incomplete, as it is relatively hard to identify these systems and constrain their parameters. The population synthesis calculations (Nelemans et al. 2005) predict many low-mass ($\sim 0.4M_\odot$) white dwarfs at $P \sim 10$ d, yet they are missing from the observational samples. Hence, larger samples of binary white dwarfs that include longer period systems are needed to definitively find a trend between orbital period and primary white dwarf mass.

All four binary systems presented in this paper will merge within a Hubble time, with total masses of $\geqslant 0.76, 0.52, 0.68,$ and $0.68M_\odot$, respectively. The quickest merger system is J1235+1543, which contains a 0.35 $M_\odot$ white dwarf with a $M \geqslant 0.17M_\odot$ companion. Note that a 0.17 $M_\odot$ companion is expected to form after the 0.35 $M_\odot$ white dwarf and it should be brighter. Hence, this is likely a low inclination system ($i \leqslant 36°$) with a companion that is comparable to or more massive than 0.35 $M_\odot$. Based on its distance of 386 pc, J1235+1543 has a gravitational wave strain of $\log h \geqslant -22.2$ at $\log \nu = -3.2$. This strain is comparable to that of the AM CVn binary GP Com. Hence, J1235+1543 is unlikely to be detected by *LISA* (Roelofs et al. 2007; Korol et al. 2017).

ACKNOWLEDGEMENTS

This work is in part supported by the NSF and NASA under grants AST-1312678, AST-1312983, and NNX14AF65G.

REFERENCES

Allende-Prieto, C., & Apogee Team 2015, American Astronomical Society Meeting Abstracts, 225, 422.07
Althaus, L. G., Miller Bertolami, M. M., & Córsico, A. H. 2013, A&A, 557, A19
Amaro-Seoane, P., Aoudia, S., Babak, S., et al. 2012, Classical and Quantum Gravity, 29, 124016
Bell, K. J., Gianninas, A., Hermes, J. J., et al. 2017, ApJ, 835, 180
Bragaglia, A., Greggio, L., Renzini, A., & D'Odorico, S. 1990, ApJ, 365, L13
Breedt, E., Steeghs, D., Marsh, T. R., et al. 2017, MNRAS, in press, arXiv:1702.05117
Brown, W. R., Kilic, M., Hermes, J. J., et al. 2011, ApJ, 737, L23
Brown, W. R., Gianninas, A., Kilic, M., Kenyon, S. J., & Allende Prieto, C. 2016, ApJ, 818, 155
Brown, W. R., Kilic, M., Kenyon, S. J., & Gianninas, A. 2016, ApJ, 824, 46
Brown, W. R., Kilic, M., Gianninas, A., ApJ, in press
Castelli, F., & Kurucz, R. L. 2004, Proceedings of the IAU Symp. No 210; Modelling of Stellar Atmospheres, eds. N. Piskunov et al. 2003, A20
Cojocaru, R., Rebassa-Mansergas, A., Torres, S., & Garcia-Berro, E. 2017, MNRAS, in press
Debes, J. H., Kilic, M., Tremblay, P.-E., et al. 2015, AJ, 149, 176
Drake, A. J., Djorgovski, S. G., Mahabal, A., et al. 2009, ApJ, 696, 870
Fontaine, G., Brassard, P., & Bergeron, P. 2001, PASP, 113, 409
Gianninas, A., Kilic, M., Brown, W. R., Canton, P., & Kenyon, S. J. 2015, ApJ, 812, 167
Hallakoun, N., Maoz, D., Kilic, M., et al. 2016, MNRAS, 458, 845
Hermes, J. J., Brown, W. R., Kilic, M., et al. 2014, ApJ, 792, 39
Hurley, J. R., Tout, C. A., & Pols, O. R. 2002, MNRAS, 329, 897
Kanaan, A., Kepler, S. O., & Winget, D. E. 2002, A&A, 389, 896
Kepler, S. O., Pelisoli, I., Koester, D., et al. 2016, MNRAS, 455, 3413
Kilic, M., Brown, W. R., Gianninas, A., et al. 2014, MNRAS, 444, L1
Kilic, M., Brown, W. R., Hermes, J. J., & Gianninas, A. 2015, Gravitational Wave Astrophysics, 40, 167
Korol, V., Rossi, E. M., Groot, P. J., et al. 2017, MNRAS, submitted, arXiv:1703.02555
Kroupa, P., & Tout, C. A. 1997, MNRAS, 287, 402
Kurtz, M. J., & Mink, D. J. 1998, PASP, 110, 934
Maoz, D., & Hallakoun, N. 2017, MNRAS, in press
Marsh, T. R., Dhillon, V. S., & Duck, S. R. 1995, MNRAS, 275, 828
Martini, P., Elias, J., Points, S., et al. 2014, Proceedings of the SPIE, 9147, 91470Z

Massey, P., Strobel, K., Barnes, J. V., & Anderson, E. 1988, ApJ, 328, 315
Maxted, P. F. L., Marsh, T. R., & Moran, C. K. J. 2000, MNRAS, 319, 305
Morales-Rueda, L., Maxted, P. F. L., Marsh, T. R., North, R. C., & Heber, U. 2003, MNRAS, 338, 752
Morales-Rueda, L., Marsh, T. R., Maxted, P. F. L., et al. 2005, MNRAS, 359, 648
Moran, C., Marsh, T. R., & Bragaglia, A. 1997, MNRAS, 288, 538
Napiwotzki, R., Yungelson, L., Nelemans, G., et al. 2004, Spectroscopically and Spatially Resolving the Components of the Close Binary Stars, 318, 402
Nelemans, G., Napiwotzki, R., Karl, C., et al. 2005, A&A, 440, 1087
Parsons, S. G., Marsh, T. R., Gänsicke, B. T., Drake, A. J., & Koester, D. 2011, ApJ, 735, L30
Press, W. H., Teukolsky, S. A., Vetterling, W. T., & Flannery, B. P. 1992, Cambridge: University Press, —c1992, 2nd ed.
Rebassa-Mansergas, A., Parsons, S. G., García-Berro, E., et al. 2017, MNRAS, 466, 1575
Roelofs, G. H. A., Groot, P. J., Benedict, G. F., et al. 2007, ApJ, 666, 1174
Saffer, R. A., Liebert, J., & Olszewski, E. W. 1988, ApJ, 334, 947
Shporer, A., Kaplan, D. L., Steinfadt, J. D. R., Bildsten, L., Howell, S. B., & Mazeh, T. 2010, ApJ, 725, L200
Tonry, J., & Davis, M. 1979, AJ, 84, 1511
Toonen, S., & Nelemans, G. 2013, A&A, 557, A87
Vennes, S., Thorstensen, J. R., Kawka, A., et al. 2011, ApJ, 737, L16
Zorotovic, M., Schreiber, M. R., Gänsicke, B. T., & Nebot Gómez-Morán, A. 2010, A&A, 520, A86
Zorotovic, M., Schreiber, M. R., Gänsicke, B. T., et al. 2011, A&A, 536, L3
Zorotovic, M., Schreiber, M. R., & Parsons, S. G. 2014, A&A, 568, L9

APPENDIX A: RADIAL VELOCITY DATA FOR FOUR BINARIES

Table A1. J0834+3049

HJD−2457000 (days)	v_{helio} (km s^{-1})
389.864816	233.3 ± 40.3
389.869532	272.5 ± 42.5
389.873496	316.3 ± 44.2
389.877461	372.8 ± 48.5
389.881431	247.0 ± 74.7
427.677917	46.5 ± 31.6
427.929727	194.4 ± 27.4
428.675806	156.7 ± 30.0
428.747331	370.1 ± 25.3
428.924687	-93.3 ± 45.7
429.694757	327.6 ± 24.1
429.711053	227.3 ± 30.8
429.738483	199.7 ± 27.9
429.902945	216.6 ± 37.5
430.721276	38.5 ± 25.8
430.759435	101.7 ± 29.2
430.836990	328.4 ± 35.2
430.920772	236.4 ± 24.1

Table A2. J1235+1543

HJD−2457000 (days)	v_{helio} (km s^{-1})
409.083366	-15.7 ± 41.2
409.084900	-82.0 ± 55.2
409.086433	-101.0 ± 33.8
409.088731	-155.7 ± 31.6
409.090264	-190.5 ± 37.0
409.091798	-92.3 ± 26.6
409.093331	-179.3 ± 28.6
409.094865	-203.0 ± 51.2
409.096398	-135.2 ± 28.5
409.097938	-157.3 ± 47.3
409.099471	-39.9 ± 36.1
427.984125	-0.8 ± 23.0
427.987065	96.7 ± 23.3
427.991093	156.0 ± 23.3
427.994080	153.2 ± 23.4
427.997043	124.2 ± 22.8
427.999994	114.7 ± 30.8
428.002992	7.5 ± 24.4
428.005932	-78.0 ± 27.3
428.009891	-132.9 ± 26.1
428.012842	-150.7 ± 25.6
428.015794	-107.2 ± 24.4
428.018769	-45.9 ± 27.0
429.002616	-136.6 ± 23.9
429.005579	-156.9 ± 22.2
429.009631	-71.3 ± 22.9
429.012594	-14.6 ± 23.9
429.983303	33.5 ± 21.9
429.986752	-24.3 ± 22.7
430.989533	-119.1 ± 22.5
430.992034	-63.1 ± 21.7
430.993608	-61.4 ± 21.6
430.995194	-11.2 ± 21.7
430.996791	36.5 ± 23.1
430.998353	109.5 ± 22.5
430.999916	143.2 ± 22.3
431.001490	156.1 ± 23.3
431.003053	188.2 ± 23.1
431.004615	185.5 ± 24.9

Table A3. J1237+4913

HJD−2457000 (days)	v_{helio} (km s^{-1})
391.101456	-176.3 ± 47.2
391.105073	-52.3 ± 43.8
391.109443	-101.3 ± 46.5
391.116495	14.4 ± 39.6
391.120112	50.2 ± 65.7
391.123731	52.9 ± 36.4
575.756677	-41.1 ± 39.1
575.763138	-100.6 ± 38.8
575.768839	-165.5 ± 41.0
575.774539	-116.7 ± 33.9
575.780997	-179.7 ± 37.2
575.786688	-153.4 ± 35.7
575.792398	-160.1 ± 34.2
575.798854	-154.0 ± 35.4
575.804554	-132.3 ± 34.4
575.810255	-155.8 ± 42.1
575.815820	-43.7 ± 45.5
580.760275	-72.1 ± 42.7
580.766731	-103.7 ± 38.5
580.772431	64.7 ± 41.8
580.778131	93.6 ± 40.7
580.784589	125.5 ± 41.0
580.790289	91.0 ± 42.5
580.795990	124.9 ± 35.9
580.802447	65.0 ± 41.5
580.808148	39.6 ± 44.1
747.010077	-55.8 ± 35.0
747.019614	-207.8 ± 36.7
747.028921	-249.9 ± 43.9
814.913842	-24.6 ± 44.1
814.981547	-3.9 ± 48.1
815.009915	147.8 ± 54.1
838.830221	-194.2 ± 37.8
838.860139	-138.1 ± 35.5
838.882893	8.4 ± 34.5
838.915161	-28.2 ± 33.8
838.940079	-131.3 ± 35.4
839.620038	-97.1 ± 36.7
839.674574	23.5 ± 34.1
839.868874	105.1 ± 33.6
840.861070	-69.6 ± 39.9

Table A4. J2342+0811

HJD−2457000 (days)	v_{helio} (km s^{-1})
582.052454	-136.3 ± 28.3
582.058911	-168.4 ± 37.0
583.040117	75.2 ± 30.7
583.046574	97.2 ± 28.3
583.052275	86.0 ± 37.6
583.057977	-38.4 ± 28.9
583.064433	-50.1 ± 38.8
691.682281	-31.5 ± 24.6
691.687605	-13.9 ± 30.2
691.733320	-118.8 ± 28.8
691.738377	-39.1 ± 34.1
691.744743	-85.6 ± 28.3
691.750495	-34.1 ± 27.9
691.757126	-14.4 ± 25.7
691.765158	32.6 ± 24.4
691.772716	42.8 ± 27.2
691.781859	70.9 ± 24.5
691.790238	147.4 ± 26.2
691.799589	126.0 ± 24.5
723.575083	31.7 ± 24.0
723.616491	-170.0 ± 32.7
723.664692	22.0 ± 24.5
723.720335	95.2 ± 26.8
723.764336	4.0 ± 58.4
724.567698	154.2 ± 28.4